Chapter 11
Patient Specific Modelling

Peter R. Hoskins, Noel Conlisk, Arjan J. Geers and Barry J. Doyle

Learning outcomes

1. Define the term 'patient specific modelling'.
2. Discuss the history of patient specific modelling.
3. Discuss the reasons for patient specific modelling gaining momentum since around 2000.
4. Describe the steps in computational mechanics (digital computation, discretization, solver).
5. Describe the steps in the patient specific modelling processing chain (imaging, segmentation, geometry preparation, meshing, computational modelling, constitutive model, boundary conditions, post-processing and display of data).
6. Describe specific examples of patient specific modelling in practice.

11.1 Introduction

11.1.1 Introduction to Patient Specific Modelling

Patient specific modelling (PSM) is concerned with the integration of data from the patient with computational modelling. The process may be imagined as a black box in which computational modelling occurs. Data from the patient is fed into the box and different types of data are outputted from the box. In the context of this book, computational modelling refers to modelling of physical phenomena, mainly

P.R. Hoskins (✉) · N. Conlisk · A.J. Geers
Edinburgh University, Edinburgh, UK
e-mail: P.Hoskins@ed.ac.uk

B.J. Doyle
University of Western Australia, Perth, Australia
e-mail: barry.doyle@uwa.edu.au

P.R. Hoskins et al. (eds.), *Cardiovascular Biomechanics*,
DOI 10.1007/978-3-319-46407-7_11

mechanical and electromagnetic forces. Similarly, inputs to computational modelling are concerned with physical phenomena; medical imaging data provides information on geometry and motion, data is provided on electrical activity from electrophysiological recordings. Other types of data concerned with patient history and 'omics' (genomics, proteomics etc.) fall under the ever growing area of big data and are not considered in this book. In the context of this book PSM may be divided into the following:

- *Electrical activity models.* These relate to modelling of electrical activity in the heart and are covered in Chap. 6.
- *0D, 1D patient specific models.* These use reduced-order models of pressure/flow in the cardiovascular system for which the 3D properties are not considered and are covered in Chap. 10.
- *3D patient specific models.* This is concerned with the integration of 3D imaging data with computational modelling of mechanical phenomena related to blood flow and cardiovascular wall motion.

This chapter is concerned with the last of these three areas; the integration of 3D imaging with computational modelling for estimation of blood flow and cardiovascular wall motion. Patient specific modelling involves a series of steps starting with image data and ending with displayed data from the modelling. These steps are referred to as a 'processing chain', 'pipeline' or 'workflow'; on the basis that information is fed in at one end of the processing chain and a great deal more information is produced at the other end of the chain. The details of the processing chain form the majority of the content of this chapter. As an introduction, the patient specific modelling processing chain can be divided into three main steps:

1. Acquisition and processing of medical imaging data
2. Computational analyses
3. Data post-processing

The computational modelling usually falls into one of two different categories; fluid mechanics or solid mechanics. Fluid mechanics applications in the cardiovascular system usually concern blood, so here PSM involves estimation of the 3D flow field. Solid mechanics applications in the cardiovascular system concern the tissues of the heart and arteries, so here PSM involves estimation of the deformation and wall stresses arising from pressure changes. Articles which review the development of PSM are by Taylor and Figueroa (2009), Hoskins and Hardman (2009), Neal and Kerckhoffs (2010) and Morris et al. (2015).

11.1.2 Terminology

As the area of PSM continues to evolve, so does the terminology. Below is a list of various terms which are used in this chapter:

Term	Definition	Comment
Idealised	Simplified representation which captures key features	Relevant for studies involving general trends
Patient specific	Values from measurement or modelling which are relevant to the individual patient	Hence can be used in diagnosis and surgical planning
Image guided modelling	Integration of imaging with computational modelling	Image data may be idealised or patient specific
Patient specific modelling	Image guided modelling which provides data relevant to the individual patient	Input data is relevant to the individual patient; hence output data can be used in diagnosis and surgical planning of the individual patient

11.1.3 History and Motivation

Numerical modelling was pioneered in the early 1950s in an attempt to better understand the vibration response of new aircraft wing designs under loading (Turner et al. 1956). The first numerical simulations involving stress in biological tissues were applied to idealised geometries in bone and teeth (Rybicki et al. 1972; Thresher and Saito 1973). The first numerical simulations of blood flow were based on idealised 2D geometries (Perktold et al. 1984; Friedman and Ehrlich 1984). The first numerical simulations to estimate cardiovascular stress were in 2D idealised arteries (Richardson et al. 1989; Loree et al. 1992; Cheng et al. 1993). Patient specific modelling has been gaining momentum since around 2000. There are four main reasons for this which are briefly outlined in this section.

Improvements in computer power. There is no doubt that the principal reason for the spread of computational modelling, not just for biomedical applications but throughout engineering and industry, has been the continued increase in computer power. Moore's law, which is that the number of transistors on an integrated circuit doubles every 2 years, has been applicable for 40 years from 1971 to 2011, with only a brief change to every 2.5 years, since 2011. In parallel to the improvements in processing power there have been reductions in price. The cost of a high-end workstation has decreased to the point where these are affordable for the individual researcher. In 2016, a high-end workstation (32-core) costs around £5000 ($8000, €7000). Three-dimensional simulations involving 500,000 nodes with time-resolved output have run times of just a few hours.

Improvements in modelling software. Early work on numerical modelling used software developed in-house. While some groups still use in-house software, commercial packages are now widely used in image guided modelling and patient specific modelling. These packages have undergone extensive validation and have options specifically designed for biomedical applications.

Availability of high-resolution medical imaging. At the beginning of the PSM processing chain is medical imaging. The modern medical imaging department has a number of 3D imaging systems with spatial resolution of around 1 mm suitable for acquiring high quality geometries for PSM.

Potential of biomechanical measurements for clinical decision-making and surgical planning. Major clinical events such as aneurysm rupture or rupture of atherosclerotic plaque are associated with mechanical failure of tissues, where tissue stress exceeds tissue strength. Growth of atherosclerotic plaque and aneurysm is associated with changes in both tissue stress and wall shear stress. This has led many groups around the world to think that measurements related to the biomechanical status of disease may provide improved diagnosis and selection of patients for treatment. Medical imaging systems are unable to measure mechanical stress, whereas stress is one of the main outputs of PSM. This has provided a key rationale for the development of PSM as a potential diagnostic tool for use in cardiovascular disease. In parallel, there has been the realisation that PSM may be used as an aid to surgical planning where, for example, the effect of different surgical approaches on the haemodynamics may be investigated in the computer first.

11.2 Computational Mechanics

11.2.1 Introduction and Rationale

It has been noted in previous chapters that there are governing equations which describe the behaviour between strain and stress in a solid and between strain rate and shear rate in a fluid. There are a very few geometries for which exact solutions of these equations exist. For a fluid, the governing equations are the 'Navier–Stokes equations'. Exact solutions of the Navier–Stokes equations may be found for simple geometries such as motion of an infinite plate and steady or pulsatile flow in a cylinder. For more complex geometries, computational mechanics provides a framework to allow the governing equations in a fluid and a solid to be solved. The mathematics of computational mechanics is complex and outside the scope of this book, but is available in standard texts and review articles for interested readers (Zienkiewicz 2004; Zienkiewicz et al. 2005; Chapra and Canale 2014). The basic steps involved in computational mechanics are detailed below:

Digital computation. The governing equations are applicable to a continuous media (i.e. all x, y, z, t). Computational mechanics operates using a digital or discrete model in which equations are solved at many specific values of x, y, z, t. This digital model is then suitable for calculation using a computer. The set of points is referred to as the 'mesh' or 'grid'. The smallest unit of the mesh is called an 'element' which consists of a number of nodes. Each node of the mesh has a number of values related to the variables in the governing equations.

Discretization. The governing equations are broken down into simpler equations which are suitable for an iterative solution using a computer. This process is called 'discretization'. There are a number of different discretization methods; 'finite element method', 'finite volume method', 'finite difference method', 'spectral element method'. These all have slight differences in the mathematical formulation and some are more suited to solid modelling while others are more suited to flow modelling.

Solver. An initial set of values is assigned to each node of the mesh. The computer programme operates in an iterative manner in which the equations at each node are solved and the set of values at each node adjusted. After several iterations, the set of values will be stabilised and the solution will be reached. It should be noted that not all solutions are physically realistic. An experienced fluid or solid mechanics specialist is required to design the mesh and prepare the simulation to avoid physically unrealistic solutions.

11.2.2 Flow and Solid Modelling

Estimation of flow field data using computational mechanics is referred to as 'computational fluid dynamics' or CFD. Commonly the finite difference and finite volume discretization methods are used in CFD software packages. Estimation of stresses in solids usually involves finite element discretization, so that solid modelling is usually referred to as 'finite element analysis' or FEA. A number of commercial packages are available for flow and solid modelling including CFX and Fluent (ANSYS, Canonsburg, PA, USA) and Abaqus (Dassault Systemes, Simulia, Rhode Island, Providence, USA). For use in blood flow, several groups have developed their own CFD packages (for example, Minev and Ethier 1998; Ethier et al. 1999; Sherwin and Karniadakis 1995; Witherden et al. 2014).

11.3 Processing Chain

This section describes the PSM processing chain (Fig. 11.1). The sections below describe each component of the chain in detail. An example of a full PSM processing chain has been described by Antiga et al. (2008).

11.3.1 Imaging

The starting point of the PSM processing chain involves the acquisition of medical imaging data. Medical imaging systems were described in Chap. 9, where it was noted that a number of imaging modalities provide high-resolution 3D data. The

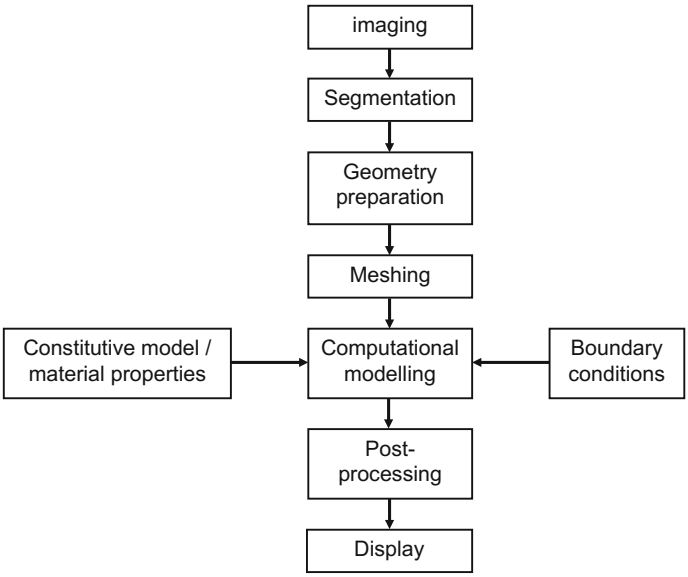

Fig. 11.1 Patient specific modelling processing chain

medical imaging dataset provides 3D data on the tissues of interest in the patient. In the case of arteries this will be the arterial wall, any thrombus (e.g. present in clinically relevant aneurysms) and the vessel lumen. The ideal imaging modality for PSM should have the following features: high resolution, low noise, artefact-free, high contrast between tissues. A brief summary of the use of different imaging modalities in PSM is described below:

Computed tomography (CT). This is the imaging modality which comes closest to the set of criteria listed above. It has been widely used in PSM of the larger arteries and of aneurysms. With multislice scanning it is possible to acquire gated 3D cardiac data from which coronary artery geometries may be obtained. Using CT it is possible to distinguish the thrombus from the lumen in aneurysms. The main limitation is the inability to measure wall thickness; this arises due to resolution limitations (around 0.6 mm) and due to insufficient contrast between the wall and surrounding soft tissue. For use in atherosclerosis, the resolution is insufficient to distinguish the detailed structure within the plaque.

Magnetic resonance imaging (MRI). Image contrast is high which enables different soft tissues to be distinguished. The good soft tissue contrast also enables some visualisation of the aortic wall, which is often not possible on CT. For use in atherosclerosis, MRI has been used to acquire 2D and 3D data in atherosclerotic plaque, where its excellent soft tissue discrimination enables visualisation of the different plaque components. However, MRI has a number of limitations for PSM. Acquisition times for 3D data can be long. For data acquired from the thorax and upper abdomen, the patient must hold their breath to limit the displacement of the

chest. Image registration tools are required to register the images together and remove this motion. MRI has much larger slice intervals compared to CT, typically around 5–6 mm for abdominal imaging protocols. So although, MRI has excellent in-plane (x, y) pixel resolution, <1 mm, the resulting geometries may lack detail in z-direction and be unsuitable for PSM.

Ultrasound. In principle, 3D ultrasound data may be acquired using externally applied transducers. However, in practice, there are problems associated with registration, low resolution, loss of data due to calcifications and bowel gas (Hammer et al. 2009). These problems are mostly resolved by the use of intravascular ultrasound where the transducer is much higher frequency (resulting in much improved spatial resolution of 50–100 μm), and where the transducer images the tissues from inside the vessel. IVUS has been used to provide 3D geometries for PSM since the very early days of PSM (Chandran et al. 1996; Krams et al. 1997). The position and orientation of the IVUS scan-plane needs to be known so that the IVUS data can be positioned within a 3D geometry. Krams et al. (1997) used an angiography system to obtain this information; the overall system was known as ANGUS (ANGiography and UltraSound).

Optical coherence tomography (OCT). This is also an invasive technique which can be used for imaging arteries and has very good spatial resolution of 10–20 μm. It was noted in Chap. 9 that the critical thickness of the cap in atherosclerotic plaque is around 70 μm, far below the resolution of CT, MRI or transcutaneous ultrasound, and the only technique capable of providing accurate measurements of cap thickness in vivo is OCT.

11.3.2 Segmentation

Segmentation is the process whereby the surfaces of the organ of interest are identified. Segmentation may also involve defining the boundaries between different regions in the organ. Typically for fluid modelling the inner lumen of the vessel is required. For solid modelling ideally both inner and outer lumen of the vessel wall should be identified. For abdominal aortic aneurysms the region of thrombus is required. For atherosclerosis, the regions need to be identified corresponding to different plaque constituents. Segmentation concerns the detection of edges in an image and is commonly used in 3D imaging for visualisation of structures. For example, in CT imaging in the Radiology Department, the soft tissues can be 'peeled back' to reveal underlying organs, skeleton etc. Segmentation can be manual, automated or semi-automated.

Manual segmentation consists of a trained operator laboriously going through each image defining the boundaries by hand. This is extremely time-consuming for the operator. Manual segmentation is still used, often when image quality is low and automated methods fail.

Threshold methods. These are the simplest automated segmentation methods and involve looking for differences in intensity values between adjacent voxels.

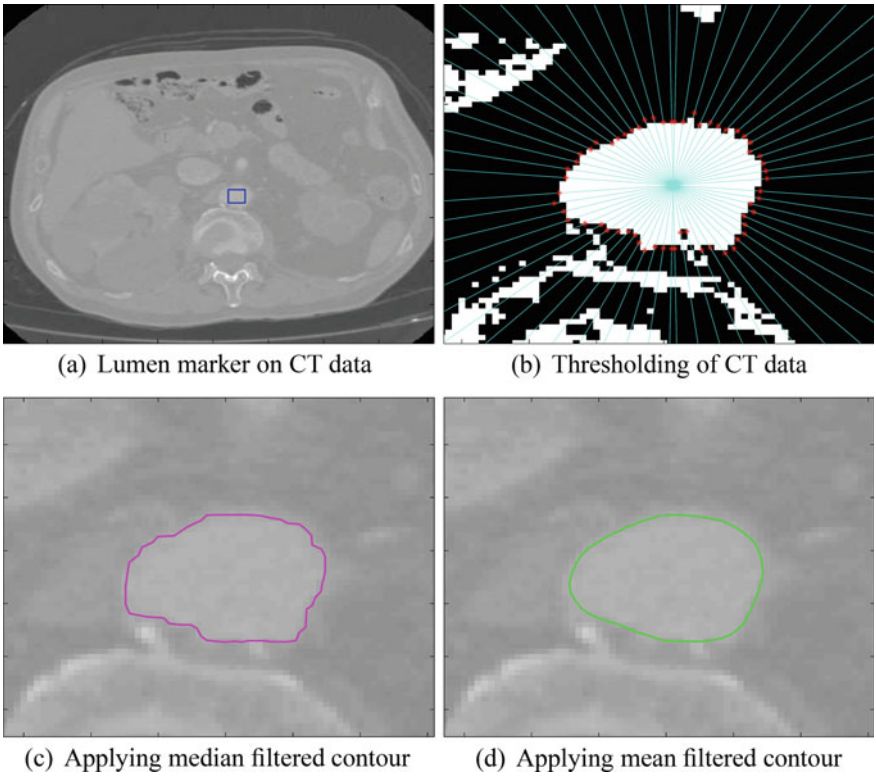

Fig. 11.2 Segmentation of the lumen of an abdominal aortic aneurysm. **a** Lumen marker is placed on the CT scan. **b** A simple threshold method is used to identify the lumen. **c** A median filter is applied to smooth the contour. **d** The contour is further smoothed using a mean filter

Figure 11.2 shows a threshold-based method in operation for identification of the inner lumen of an abdominal aortic aneurysm in a CT dataset. The algorithm starts in the middle of the lumen and works outwards radially. When the intensity value exceeds a threshold value, the edge has been found. These simple methods work best when image noise is low. Some commercial software such as Mimics (Materialise, Belgium) allows manual definition of the organ boundaries which are then smoothed to produce a 3D surface mesh suitable for modelling.

Deformable models. These are often referred to as 'active contours' (2D), 'active surfaces' (3D) or 'snakes' (Xu et al. 2000). These provide a widely used and powerful segmentation technique. The snake is a connected set of points which can deform dependent on the local image content. Typically an initial contour is seeded and grows outwards until it reaches the organ boundary. Local image measures which have high values where there is an edge are used to constrain the snake. The snake will often be 'trained' from learning datasets to exhibit some sort of geometrical behaviour, e.g. when segmenting the left ventricle the snake knows

roughly what shape a typical left ventricle is and this is used as a constraint in the process. The result from this approach is a robust 3D reconstruction with good reproducibility.

Automatic segmentation methods represent the ideal scenario for the operator. These work best when the image quality is very good such as for CT images. Automated segmentation techniques can be difficult to develop, especially when the image quality is poor. If the information required for segmentation is not present in the image then no amount of processing will help and the best that can be done is a 'best guess', either by the automated software or by the operator. Usually segmentation in PSM is done as a combination of automated and manual input.

11.3.3 Geometry Preparation

Prior to meshing, the surfaces obtained from segmentation must be prepared. For flow modelling, the blood is only in contact with the inner surface of the vessel. In this case, a single layer surface will suffice. For solid modelling in a vessel both an inner and outer surface are required. Due to imaging constraints, especially in CT, it is often not possible to identify the outer surface of the vessel. In this case, it is commonly assumed that the vessel has a particular wall thickness. In the case of abdominal aortic aneurysm, it is common to assume that the wall has a constant thickness of 1.9 mm (Raghavan et al. 2000), or that the wall thickness varies between 1.5 and 1.13 mm at thrombus-free and covered sites respectively (Gasser et al. 2010). The surfaces of resulting geometries must be smoothed to remove artefacts of the reconstruction algorithm and to ensure that surfaces do not cause undesirable issues during the meshing or modelling stages.

11.3.4 Meshing

Meshing is the process where the 3D segmented geometry is divided into many elements (Figs. 11.3 and 11.4). Mesh generation is one of the critical parts of the patient specific modelling process. Increased solution accuracy is produced with a larger number of elements, but at the expense of increased processing time. The total number of elements employed for a given model is a balance between solution accuracy and processing time. While the mesh is generated using a specialist computer programme, the operator has considerable input in defining element types and element sizes. For example, when there are large velocity gradients or stress gradients then the mesh density needs to be higher. The process of mesh optimisation is therefore essential and involves adjusting the local mesh following examination of the solution. In practice, several iterations between mesh and solution may be required.

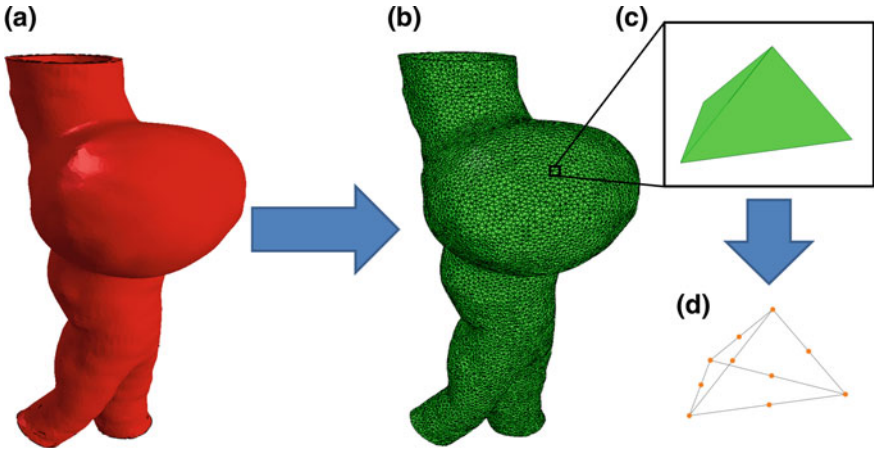

Fig. 11.3 Meshing of an abdominal aortic aneurysm geometry. **a** Reconstructed geometry from CT data. **b** Volume mesh. **c** Tetrahedral element. **d** Close up showing position of the 10 nodes

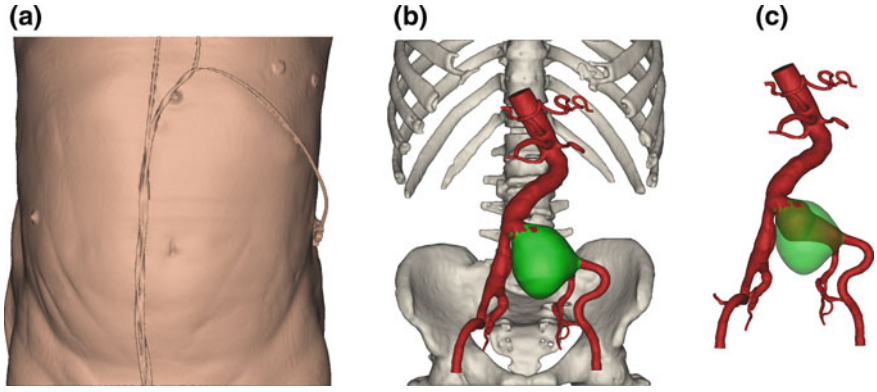

Fig. 11.4 Typical 3D reconstruction based on the marching squares/cubes algorithm in Mimics v18 (Materialise, Belgium). **a** The entire torso with external leads. **b** The main features of the skeleton. **c** The abdominal aorta with infrarenal and renal branches, iliac bifurcation, common iliac arteries and internal/external iliac arteries. This case shows a 91 year old female with an isolated common iliac artery aneurysm and thrombus (*green*)

Different types of element may be used. Common elements are tetrahedron (shaped like a pyramid) or hexahedron (shaped like a brick). Meshes may involve both types of elements. Hexahedral elements are generally more suited to structures with straight edges, hence in PSM the use of tetrahedral elements is more common. For CFD, some codes such as STAR-CCM+ (CD-adapco Group) use polyhedral elements which offer improved computation time over tetrahedral elements, while maintaining the flexibility of tetrahedral elements to mesh complex geometries.

11.3.5 Computational Modelling

The next stage is computational modelling in which the solution is produced after several iterations. A number of different modelling regimes can be adopted. Computational fluid dynamics can be performed using a rigid-walled approach, which is simple and sufficient for providing output data on basic haemodynamics. A moving-wall method can be adopted with input of moving-wall geometry data. Solid modelling is used for estimation of tissue stress. Solid modelling alone is suitable for estimation of tissue stress in abdominal aortic aneurysms and for 2D studies in atherosclerotic plaque. Combined solid-fluid modelling is called fluid structure interaction or FSI. This is needed when the pressure distribution is not uniform within the 3D geometry and is essential for 3D studies of tissue stress in stenosed arteries.

More advanced modelling regimes have been developed for use in research. These include inverse methods which have been used to account for pre-stressing (Gee et al. 2009) and to estimate patient specific material properties (Chandran et al. 2003; Baldewsing et al. 2008).

11.3.6 Constitutive Model

The computational model needs to account for the governing physical behaviour of the solid or fluid. For blood, it is common to assume that blood is Newtonian, especially in the larger arteries. However, non-Newtonian behaviour can also be assigned. For modelling of the vessel wall, it is common to use a hyperelastic model (described in Chap. 1).

11.3.7 Boundary Conditions

The boundary conditions are the set of additional constraints which are required for modelling.

For CFD in a rigid-walled non-bifurcating vessel, it is sufficient to specify the inlet flow-time waveform; pressure is not needed. It is common to add an extension pipe to the inlet to allow the flow to become fully developed at the true inlet to the vessel. Information on blood velocity in the individual patient can be obtained from Doppler ultrasound or MRI (Figs. 11.5 and 11.6). For Doppler ultrasound, the maximum velocity–time waveform may be obtained and converted to a flow-time waveform using Womersley equations (Blake et al. 2008). For MRI, a 2D velocity profile may be obtained, with either 1 or 3 velocity components. The use of 3 components allows rotational flow at the inlet to be accounted for. The use of

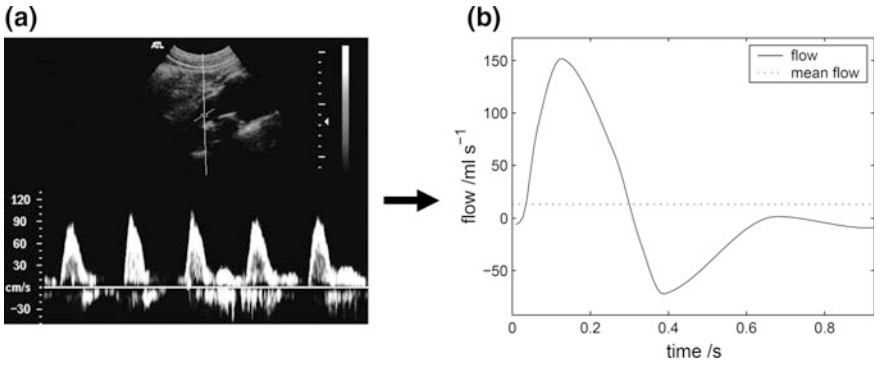

Fig. 11.5 Use of Doppler ultrasound to obtain inlet flow data. This example is from a patient with an abdominal aortic aneurysm. **a** Doppler ultrasound velocity–time waveforms and **b** estimated flow-time waveform

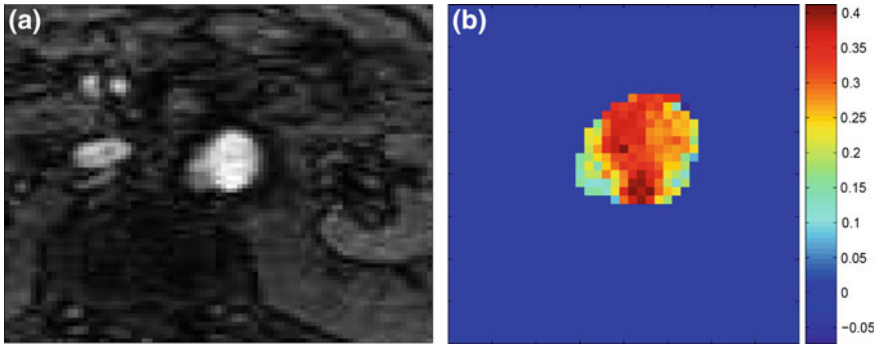

Fig. 11.6 Measurement of the 2D velocity profile using MRI in the abdominal aorta. **a** MRI images and **b** 2D velocity profile

different inlet flows does have a significant impact on the calculated flow patterns as shown in Fig. 11.7.

Further information is needed for CFD if there is a bifurcation. Ideally, 3D-models should be coupled to 0D- or 1D-models representing the rest of the circulation in order to obtain accurate estimations of the pressure field (Blanco et al. 2009; Kim et al. 2010). In some fields of research, however, simulations still predominantly make use of a rigid wall assumption, a flow rate waveform at the inlet, and zero pressure conditions at the outlets. This has led to a strong emphasis on wall shear stress over pressure in hemodynamic studies of, for example, cerebral aneurysms (Taylor and Figueroa 2009).

Pressure information may be obtained non-invasively using a monitor with an arm cuff which is applicable for PSM in the brachial artery. Obtaining pressure information for other arteries non-invasively is more difficult and it is common to make assumptions; e.g. simply using the pressure from the arm cuff.

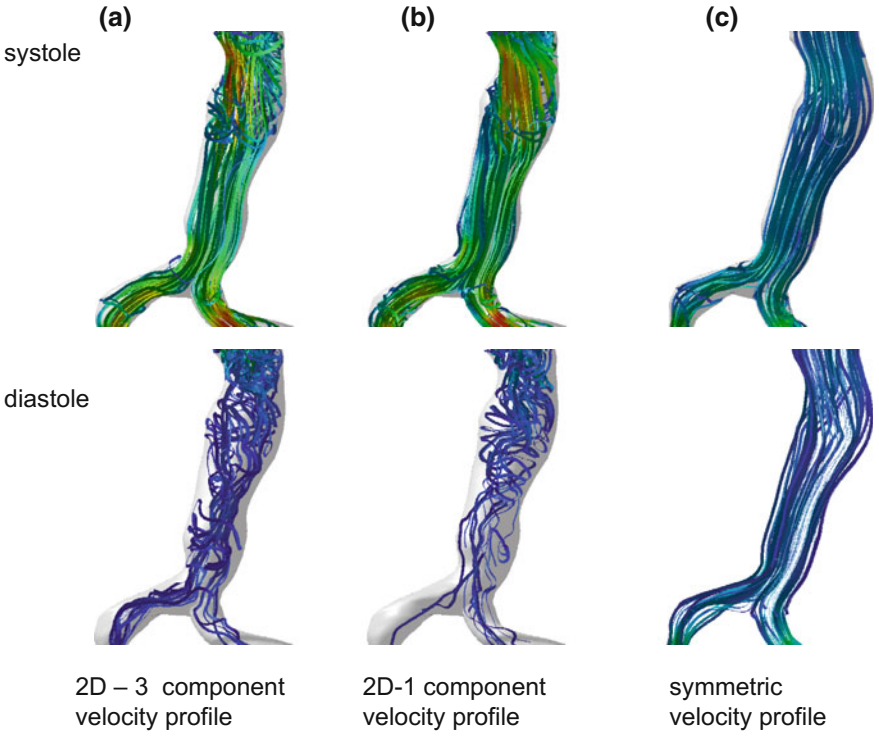

Fig. 11.7 Differences in flow patterns arising from different inlet flows. **a** 2D velocity profile with 3 velocity components, **b** 2D velocity profile with 1 velocity (z) component and **c** axisymmetric profile generated from maximum velocity data

Additional information on the pattern of loading is also required for the purposes of solid modelling. Loading can be static or dynamic and may be uniformly distributed over the faces of multiple elements in the mesh or applied as concentrated forces at a select group of nodes. For example, in FEA models of abdominal aortic aneurysms loading representative of peak systolic blood pressure, 120 mm Hg (0.016 MPa), is typically applied as an outward facing uniformly distributed pressure load acting on the inner luminal surface of the aneurysm

Consideration of realistic geometry, material properties, boundary conditions and loading are essential in order to obtain accurate results from any FE analysis.

11.3.8 Post-processing

Post-processing is concerned with calculation of relevant quantities from the data. Examples would be wall shear stress or particle paths. Post-processing also involves the creation of image and video files for display.

11.3.9 Display of Data

The final data is displayed on the computer screen, as a video for time-resolved data or as individual images. As the data is 3D the display may be a projection of the 3D dataset from one viewpoint. Several different displays may be used. Figure 11.8 shows display modes for CFD; streamlines for visualisation of overall flow patterns, velocity profiles to examine for asymmetry of flow and wall shear stress.

11.4 Patient Specific Modelling in Practice

This section will describe specific examples of PSM in different vessels drawn from the literature. It is noted that the technical level of material in this section is higher than the rest of the book in order to show how PSM is performed in practice.

11.4.1 Flow in a Cerebral Aneurysm

Patient specific modelling of cerebral aneurysms has focused on the role of haemodynamics in the development and rupture of cerebral aneurysms and the haemodynamic effect of endovascular treatment (Cebral et al. 2011; Larrabide et al. 2013). To illustrate the typical modelling pipeline of this application, we will discuss the details of the pipeline used in Geers et al. (2011). The main steps are visualised in Fig. 11.9.

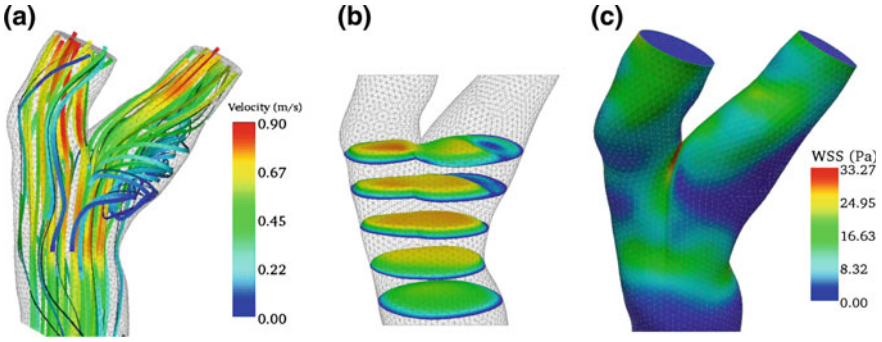

Fig. 11.8 Different display modes for CFD; **a** streamlines, **b** 2D velocity profiles **c** wall shear stress. Reprinted from Ultrasound in Medicine and Biology, Vol. 35(12), Hammer S, Jeays A, MacGillivray TJ, Allan PL, Hose R, Barber D, Easson WJ, Hoskins PR; Acquisition of 3D arterial geometries and integration with computational fluid dynamics; pp. 2069–2083, Copyright (2009), with permission from the World Federation for Ultrasound in Medicine & Biology

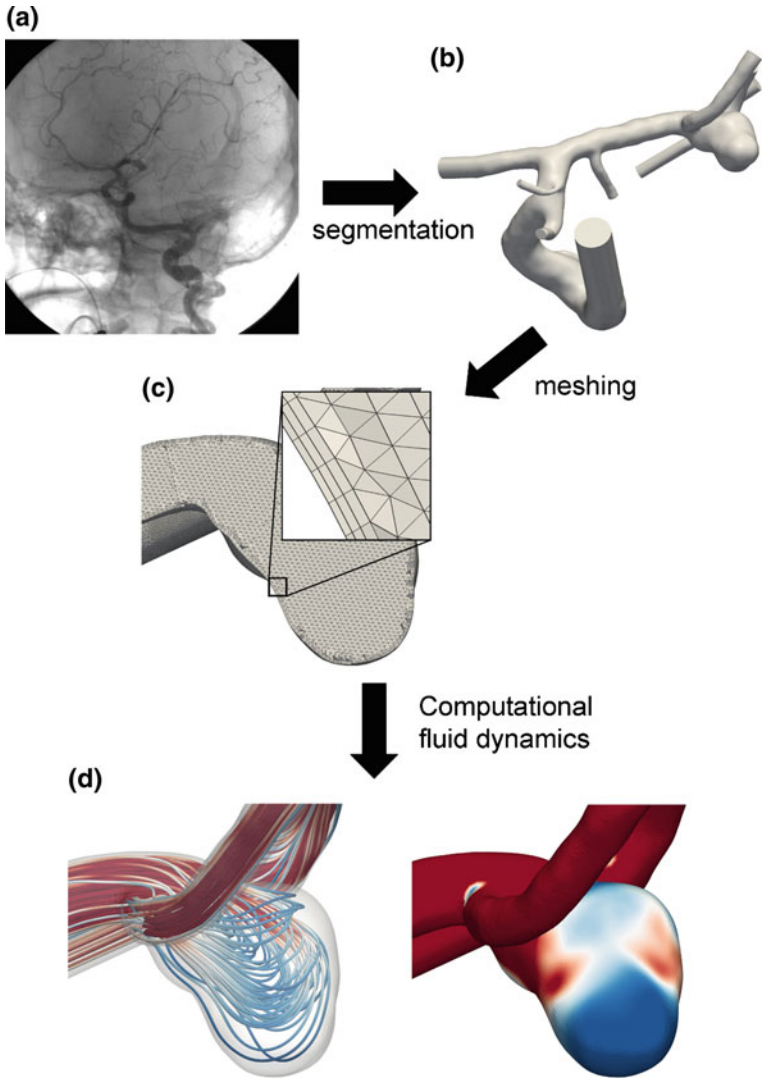

Fig. 11.9 Cerebral aneurysm CFD. **a** Rotational angiography image of the skull. Cerebral aneurysm, **b** Segmented geometry, **c** Meshed geometry close up **d** Flow streamlines and wall shear stress

Patient specific vascular models, represented by triangular surface meshes, were constructed by segmenting 3D rotational angiography (3DRA) images using a geodesic active regions approach (Bogunovic et al. 2011). Manual post-processing

operations were applied to separate touching vessels, extrude poorly segmented in- and outlets, smooth the surface and improve the mesh quality. Operations were performed in ReMESH v2.0 (IMATI-GE/CNR, Genova, Italy) (Attene et al. 2006).

Unstructured volumetric meshes were created with ICEM CFD 13.0 (ANSYS, Canonsburg, PA, USA) using an octree approach. Meshes were composed of tetrahedral elements with a side length of 0.2 mm and three prism layers with a total height of 0.15 mm. The prism layers covered the vessel wall to locally ensure an accurate definition of the velocity gradient for the computation of the wall shear stress.

CFD simulations were created with CFX 13.0 (ANSYS), which is a commercial vertex-centered finite volume solver. Blood was modelled as an incompressible Newtonian fluid with density of 1060 kg m^{-3} and viscosity of 4 mPa s. Vessel walls were assumed rigid with a no-slip boundary condition. A straight inlet extension was added to the image-based vasculature, and a parabolic velocity profile was imposed at the inlet of the extension.

Since patient specific flow information was unavailable the flow rate waveform at the inlet was estimated, and zero pressure boundary conditions were imposed at all outlets. The shape of the flow rate waveform was obtained from phase-contrast MR data of a healthy volunteer. The time-averaged flow rate was chosen to obtain a physiologically realistic mean wall shear stress of 1.5 Pa near the inlet. The cardiac cycle was discretised in time steps of 0.003 s around peak systole, when the time-derivative of the flow rate is relatively large, and 0.02 s elsewhere. Figure 11.10 shows the swirling flow patterns and reduced shear stress within the aneurysm.

11.4.2 2D Stress Estimation in an Atherosclerotic Plaque

Early work on patient specific modelling of stress in atherosclerotic plaque obtained 2D cross sectional microscopy images from autopsy specimens (Cheng et al. 1993). These showed stress 'hot spots' in the thin fibrous cap, leading to the hypothesis that plaque rupture where stress is high (further discussed in Chap. 15). In vivo PSM of stress estimation in plaque involves the use of high-resolution non-invasive imaging. MRI was used to obtain 2D data on plaque composition and estimated tissue stress using FEA (Li et al. 2006). The artery was segmented manually into four regions (wall, lumen, lipid pool, fibrous cap), and a B-spline fitting procedure used to generate the final geometry for meshing. Material properties were assigned based on a 2-term strain energy model:

$$W = \sum_{i=1}^{N} \frac{\mu_i}{\alpha_i} J^{-\frac{\alpha_i}{3}} \left(\lambda_1^{\alpha_i} + \lambda_2^{\alpha_i} + \lambda_3^{\alpha_i} - 3\right) + 4.5\left(K^{-\frac{1}{3}} - 1\right)^2,$$

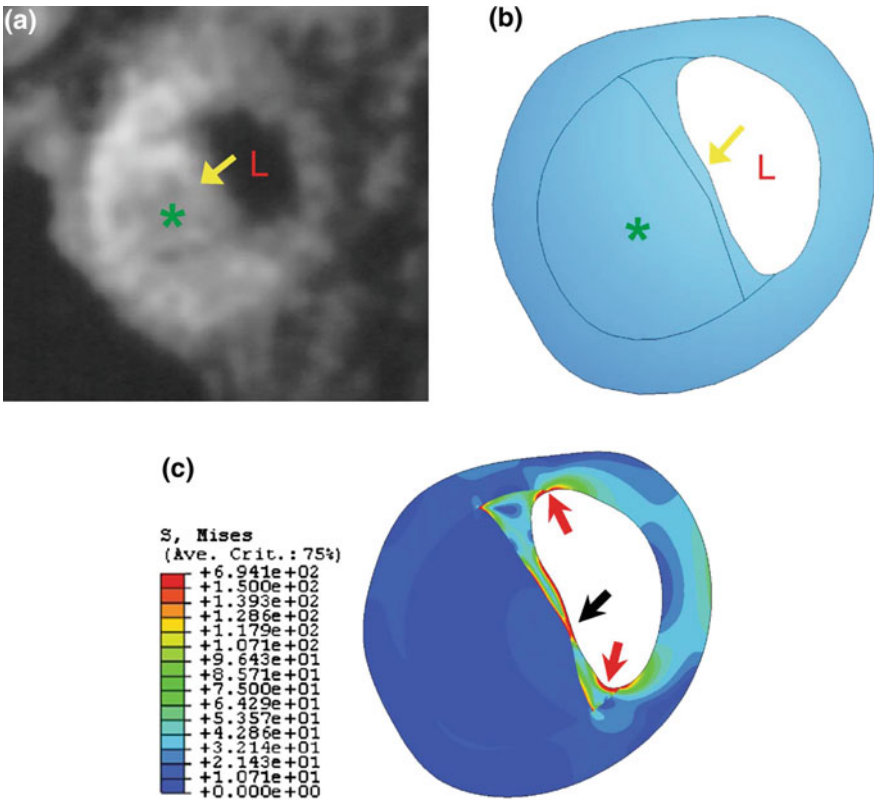

Fig. 11.10 Estimation of 2D stress in an atherosclerotic plaque with the lumen (*L*), cap (*arrow*) and lipid pool highlighted (*). **a** MRI scan of the plaque, **b** Segmented image **c** Image of von Mises stress. Reprinted from Journal of Biomechanics, Vol. 39(14), Li ZY, Howarth S, Trivedi RA, U-King-Im JM, Graves MJ, Brown A, Wang L, Gillard JH; pp. 2611–2622, Copyright (2006), with permission from Elsevier

where N is the number of terms taken to be 2. λ_1 is the principle stretch ratio, J is the determinant of the deformation gradient tensor and K the bulk modulus. μ_i are moduli constants and $\mu_1 = -\mu_2$. α_i are exponent constants and $\alpha_1 = -\alpha_2$. Values used are shown in Table 11.1.

Tonometry was used to obtain an uncalibrated pressure waveform. Pressure values were assigned corresponding to 115 mmHg mean pressure and 60 mmHg pulse pressure. Meshes were generated with an average element dimension of 0.1 mm. Solid modelling was performed using an FEA package (Abaqus software V6.5, Rhode Island, Providence, USA). Von Mises stress was displayed using Abaqus post-processing.

Figure 11.10 shows a cross section of the artery from MRI, the segmented geometry and the tissue stress distribution with hot spots at the shoulders of the fibrous cap and in the mid section.

Table 11.1 The parameters used for the plaque components and the vessel wall in the Ogden model

Tissues properties	μ_1	μ_2	α_1	α_2	K (Mpa)
Vessel wall	0.0008	−0.0008	30	−30	1600
Fibrous cap	0.0015	−0.0015	30	−30	3000
Lipid pool	0.0001	−0.0001	27	−27	200

11.4.3 3D Stress Estimation in an AAA

Early work on 3D stress estimation in abdominal aortic aneurysms was performed by Raghavan et al. (2000). Since then several groups have reported 3D stress estimation, discussed in detail in Chap. 16. The workflow described here is based on work undertaken in Edinburgh.

Computed tomography (CT) was used to obtain a high-resolution image stack of a patient specific abdominal aortic aneurysm (AAA) from the MA^{3}RS clinical trial database (McBride et al. 2015). The region of interest spanned from above the renal arteries to just below the iliac bifurcation (Aquilion One, Toshiba Medical Systems Ltd, UK), the slice thickness was 1 mm, with a pixel size of 0.625 mm.

Segmentation and 3D reconstruction was performed using commercial software (A4 Clinics Research Edition, VASCOPS GmbH, Sweden). The luminal region was segmented automatically using a 2D snake approach, and the outer wall was segmented using a 3D deformable balloon model initiated from the luminal surface. Manual correction of the outer wall contours was carried out on slices, where the automatic algorithms failed to distinguish a clear boundary with the surrounding tissue. Following generation of the outer wall the software then captures the wall-thrombus interface. Rather than assuming a uniform wall thickness of 1.5 mm, this package employs a specialist algorithm to calculate a more physiological aneurysm wall thickness distribution, which varies between 1.5 and 1.13 mm at the thrombus-free and covered sites, respectively (Gasser et al. 2010).

Finite element (FE) meshes were then created from the three-dimensional aneurysm geometry using the A4 clinics research software (VASCOPS), after suitable refinement the meshes typically consisted of >140,000 hexahedral elements (C3D8H). The refined meshes were then exported to Abaqus 6.10-1 (Dassault Systemes, Simulia, Providence, RI, USA) for analysis.

In the present study, both the aortic wall and intraluminal thrombus regions were modelled as hyperelastic, homogeneous, incompressible and isotropic materials, using well established constitutive models with material constants based on population data (Raghavan et al. 2000; Wang et al. 2001). Loading representative of peak systolic blood pressure, 120 mm Hg (0.016 MPa), was applied as an outward facing uniformly distributed pressure load acting on the luminal surface of the aneurysm. The effect of wall shear stress due to blood flow was not considered due to its negligible magnitude. Residual stresses in the aortic wall itself, and the interaction of the aorta with the surrounding structures of the body (e.g. organs and

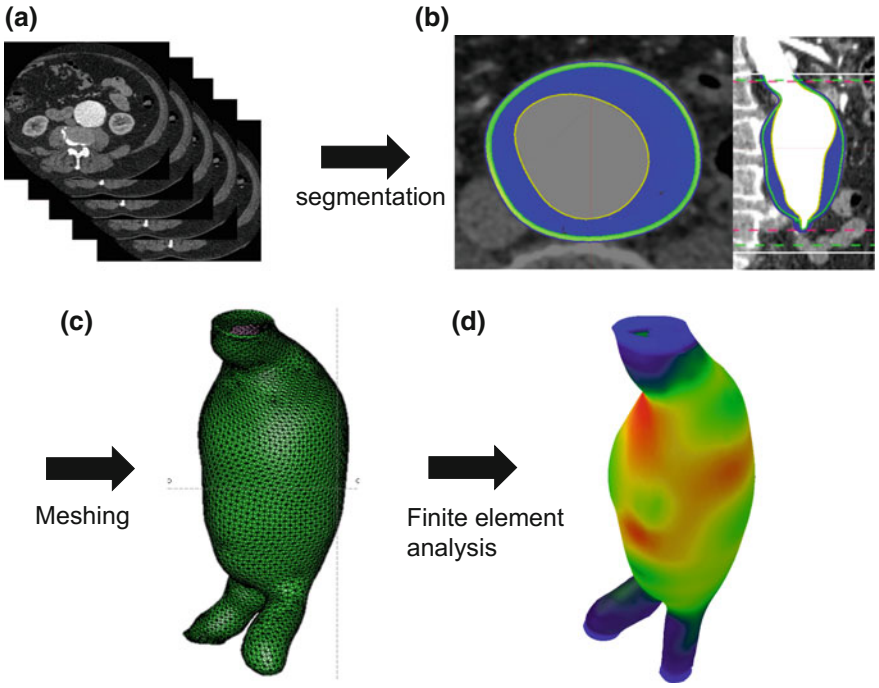

Fig. 11.11 Abdominal aortic aneurysm FEA. **a** CT slices of the aneurysm, **b** Wall and thrombus segmented, **c** Volume mesh **d** Stress estimated using FEA

spine), were also not considered; however, displacements at the distal and proximal most regions of each aneurysm were restrained, in all degrees of freedom, to model attachment of the AAA to the rest of the aorta.

Contour plots of the resulting von Mises stress distributions were then visualised using Abaqus/CAE, as shown in Fig. 11.11.

11.4.4 3D Stress Estimation in an Atherosclerotic Plaque

Section 11.4.2 described 2D stress estimation. Later work from the same group described 3D PSM of atherosclerotic plaque in the carotid bifurcation (Gao et al. 2011). 3D ECG-gated data was obtained from MRI, along with inlet time-varying velocity data. In-house software was created with Matlab to perform manual segmentation on a series of 2D slices; segmenting the lipid core, the arterial wall and lumen (Fig. 11.12). A 3D plaque geometry was constructed from the segmented 2D slices using Solidworks with surface smoothing. A 10 % shrinkage was applied to mimic the stress-free state. An FSI modelling regime was used. For the solid model assumptions were made of incompressibility, isotropy and nonlinearity for the carotid wall. A nonlinear strain energy function was used with parameters described in Gao et al.

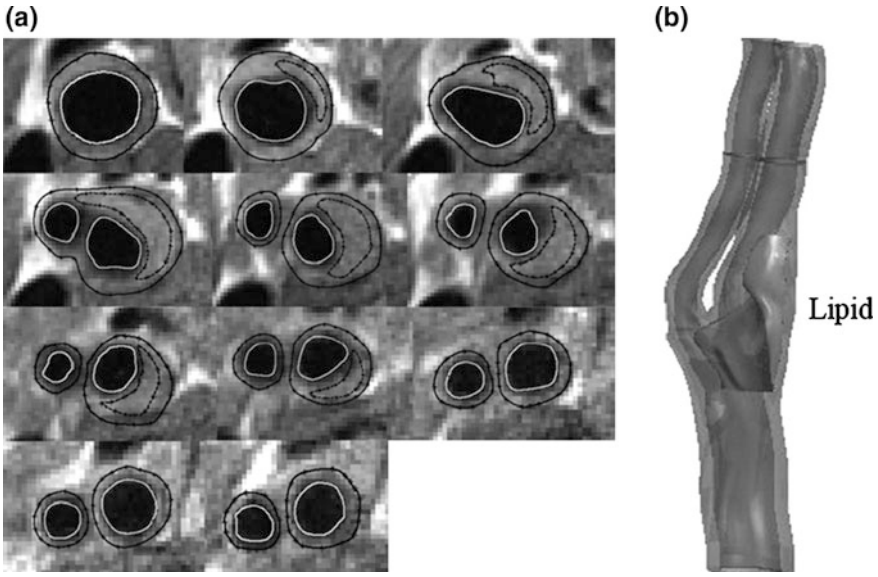

Fig. 11.12 **a** Sequential MRI slices from a carotid bifurcation with atherosclerosis with segmentation of inner and outer lumen and lipid pool. **b** Reconstructed geometry of the carotid bifurcation. Reprinted from Journal of Biomechanics, Vol. (44), Gao H, Long Q, Kumar Das S, Halls J, Graves M, Gillard JH, Li ZY; Study of carotid arterial plaque stress for symptomatic and asymptomatic patients; pp. 2551–2557, Copyright (2011), with permission from Elsevier

(2011). The solid modelling mesh consisted of 90,000 10-node tetrahedral elements. For fluid modelling, the mesh consisted of 1 million 4-node tetrahedral elements. Blood was modelled as a Newtonian incompressible fluid with a viscosity of 4 mPa s with a density of 1067 kg m^{-3}. Mass flow rates at the common (CCA) and internal carotid artery (ICA) were obtained from MRI. Mass flow rate in the external carotid artery (ECA) was obtained as the difference between CCA and ICA. CFD simulations were performed to obtain pressure–time curves which were scaled with a physiologic range of 80–110 mmHg. Fully coupled FSI was undertaken for stress analysis; CFD was used to estimate pressure values which were passed to FEA from which displacement was estimated. Displacement values were used to adjust the 3D geometries and a further iteration of CFD/FEA performed. This continued until all fields and loads converged. The final output was the 3D pressure and stress (Fig. 11.13).

11.4.5 Patient Specific Modelling Without PSM-Specific Material Properties

There is considerable variation between material properties measured from patient to patient, and the typical assumptions used in stress modelling that patients have similar material properties impacts the usefulness of the approach. Readers with a

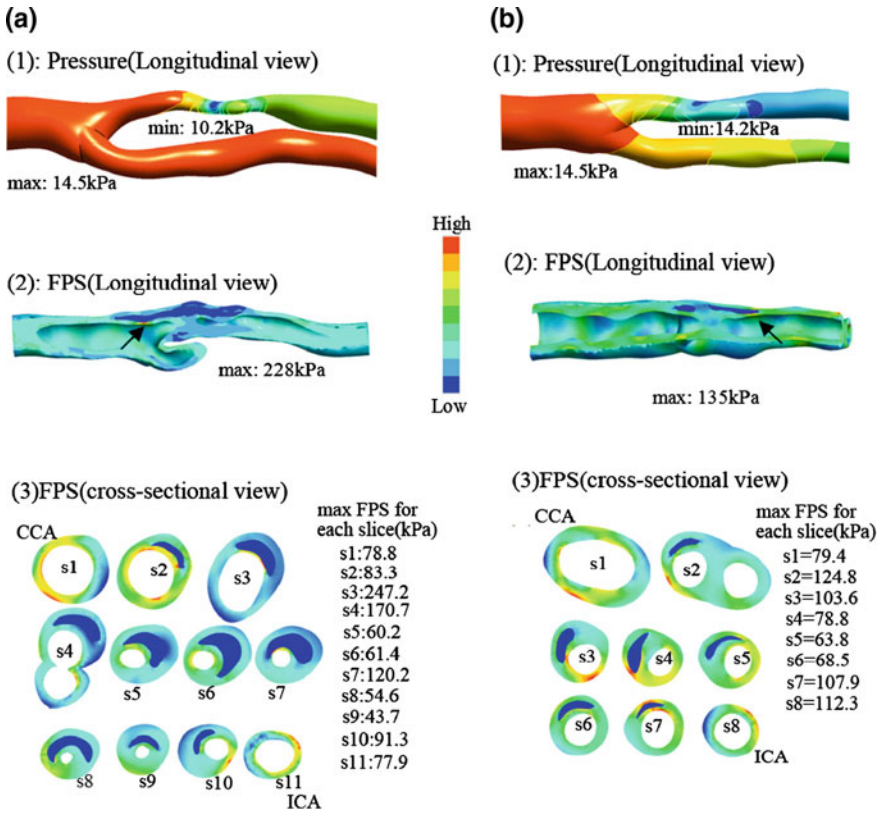

Fig. 11.13 Pressure and wall stress in the carotid bifurcation estimated using computational modelling, where there is atherosclerotic narrowing in the internal carotid artery using the geometries shown in Fig. 11.12. Reprinted from Journal of Biomechanics, Vol. (44), Gao H, Long Q, Kumar Das S, Halls J, Graves M, Gillard JH, Li ZY; Study of carotid arterial plaque stress for symptomatic and asymptomatic patients; pp. 2551–2557, Copyright (2011), with permission from Elsevier

background in engineering mechanics may be familiar with statically determinate structures. Such structures are ones in which the reactions and internal forces can be solely determined from equations of equilibrium. What this means is that results of stress analyses are independent of material properties. In practice, this means that computational models reconstructed from medical images of a living patient are reconstructions of a loaded geometry as the vessel is already subjected to internal pressurisation. Taking advantage of this enables stress analysis to be performed on multi-material vessel structures, so long as sensible ratios of stiffness between materials is maintained. This approach eliminates the inter-patient variability of material properties. This is an emerging area of research and applicable to a wide range of patient specific modelling scenarios (Miller and Lu 2013; Joldes et al. 2009).

References

Antiga L, Piccinelli M, Botti L, Ene-Iordache B, Remuzzi A, Steinman DA. An image-based modeling framework for patient-specific computational hemodynamics. Med Biol Eng Comput. 2008;46:1097–112.

Attene M, Falcidieno B. ReMESH: an interactive environment to edit and repair triangle meshes. In: Proceedings IEEE international conference on shape modeling and applications 2006 (SMI'06); 2006. p. 271–6.

Baldewsing RA, Danilouchkine MG, Mastik F, Schaar JA, Serruys PW, van der Steen AFW. An inverse method for imaging the local elasticity of atherosclerotic coronary plaques. IEEE Trans Informat Technol Biomed. 2008;12:277–89.

Blanco PJ, Pivello MR, Urquiza SA, Feijoo RA. On the potentialities of 3D-1D coupled models in hemodynamics simulations. J Biomech. 2009;42:919–30.

Blake JR, Meagher SC, Fraser KH, Easson WJ, Hoskins PR. A method to estimate wall shear rate with clinical ultrasound scanners. Ultrasound Med Biol. 2008;34:760–74.

Bogunovic HJ, Pozo M, Villa-Uriol MC, Majoie CB, van den Berg R, van Andel HAFG, Macho JM, Blasco J, San Roman L, Frangi AF. Automated segmentation of cerebral vasculature with aneurysms in 3DRA and TOF-MRA using geodesic active regions: an evaluation study. Med Phys. 2011;38:210–22.

Cebral JR, Mut F, Weir J, Putman CM. Quantitative characterization of the hemodynamic environment in ruptured and unruptured brain aneurysms. AJNR Am J Neuroradiol. 2011;32:145–51.

Chandran KB, Vonesh MJ, Roy A, Greenfield S, Kane B, Greene R, McPherson DD. Computation of vascular flow dynamics from intravascular ultrasound images. Med Eng Phys. 1996;18:295–304.

Chandran KB, Mun JH, Choi KK, Chen JS, Hamilton A, Nagaraj A, et al. A method for in-vivo analysis for regional arterial wall material property alterations with atherosclerosis: preliminary results. Med Eng Phys. 2003;25:289–98.

Chapra S, Canale R. Numerical methods for engineers. 7th ed. New York: McGraw-Hill; 2014.

Cheng GC, Loree HM, Kamm RD, Fishbein MC, Lee RT. Distribution of circumferential stress in ruptured and stable atherosclerotic lesions—a structural-analysis with histopathological correlation. Circulation. 1993;87:1179–87.

Ethier CR, Steinman DA, Ojha M. Comparisons between computational hemodynamics, photochromic dye flow visualization and magnetic resonance velocimetry. In: Collins MW, Xu Y, editors. Hemodynamics of internal organs. Southampton: WIT Press; 1999. p. 131–83.

Friedman MH, Ehrlich LW. Numerical simulation of aortic bifurcation flows: the effect of flow divider curvature. J Biomech. 1984;17:881–8.

Gao H, Long Q, Kumar Das S, Halls J, Graves M, Gillard JH, Li ZY. Study of carotid arterial plaque stress for symptomatic and asymptomatic patients. J Biomech. 2011;44:2551–7.

Gasser TC, Auer M, Labruto F, Swedenborg J, Roy J. Biomechanical rupture risk assessment of abdominal aortic aneurysms: model complexity versus predictability of finite element simulations. Eur J Vasc Endovasc Surg. 2010;40:176–85.

Gee MW, Reeps C, Eckstein HH, Wall WA. Prestressing in finite deformation abdominal aortic aneurysm simulation. J Biomech. 2009;42:1732–9.

Geers AJ, Larrabide I, Radaelli AG, Bogunovic H, Kim M, van Andel HAFG, Majoie CB, VanBavel E, Frangi AF. Patient-specific computational hemodynamics of intracranial aneurysms from 3D rotational angiography and CT angiography: an in vivo reproducibility study. Am J Neuroradiol. 2011;32:581–6.

Hammer S, Jeays A, MacGillivray TJ, Allan PL, Hose R, Barber D, Easson WJ, Hoskins PR. Acquisition of 3D arterial geometries and integration with computational fluid dynamics. Ultrasound Med Biol. 2009;35(12):2069–83.

Hoskins PR, Hardman D. 3D imaging and computational modelling for estimation of wall stress in diseased arteries. Brit J Radiol. 2009;82:S3–17.

Joldes GR, Miller K, Wittek A, Doyle BJ. A simple,effective and clinically-applicable method to compute abdominal aortic aneurysm wall stress. J Mech BehavBiomed Mat. 2016;58:139–48

Kim HJ, Vignon-Clementel IE, Coogan JS, Figueroa CA, Jansen KE, Taylor CA. Patient-specific modeling of blood flow and pressure in human coronary arteries. Ann Biomed Eng. 2010;38:3195–209.

Krams R, Wentzel JJ, Oomen JAF, Vinke R, Schuurbiers JCH, de Feyter PJ, Serruys PW, Slager CJ. Evaluation of endothelial shear stress and 3D geometry as factors determining the development of atherosclerosis and remodeling in human coronary arteries in vivo—combining 3D reconstruction from angiography and IVUS (ANGUS) with computational fluid dynamics. Arterioscler Thromb Vasc Biol. 1997;17:2061–5.

Larrabide I, Aguilar ML, Morales HG, Geers AJ, Kulcsar Z, Rufenacht DA, Frangi AF. Intra-aneurysmal pressure and flow changes induced by flow diverters: relation to aneurysm size and shape. Am J Neuroradiol. 2013;34:816–22.

Li ZY, Howarth S, Trivedi RA, U-King-Im JM, Graves MJ, Brown A, et al. Stress analysis of carotid plaque rupture based on in vivo high resolution MRI. J Biomech. 2006;39(14): 2611–22.

Loree HM, Kamm RD, Stringfellow RG, Lee RT. Effects of fibrous cap thickness on peak circumferential stress in model atherosclerotic vessels. Circ Res. 1992;71:850–8.

McBride OMB, Berry C, Burns P, Chalmers RTA, Doyle B, Forsythe R, Garden OJ, Goodman K, Graham C, Hoskins P, Holdsworth R, MacGillivray TJ, McKillop G, Murray G, Oatey K, Robson JMJ, Roditi G, Semple S, Stuart W, van Beek EJR, Vesey A, Newby DE. MRI using ultrasmall superparamagnetic particles of iron oxide in patients under surveillance for abdominal aortic aneurysms to predict rupture or surgical repair: MRI for abdominal aortic aneurysms to predict rupture or surgery—the MA3RS study. Open Heart 2015;2:2. doi:10.1136/openhrt-2014-000190.

Miller K, Lu J. On the prospect of patient-specific biomechanics without patient-specific properties of tissues. J Mech Behav Biomed Mater. 2013;27:154–66.

Minev PD, Ethier CR. A characteristic/finite element algorithm for the Navier-Stokes equations using unstructured grids. Comput Meth Appl Mech Engng. 1998;178:39–50.

Morris PD, Narracott AJ, von Tengg-Koblingk H, Silva Soto DA, Hsiao S, Lungu A, Evans P, Bressloff NW, Lawford PV, Hose DR, Gunn JP. Computational fluid dynamics modelling in cardiovascular medicine. Heart 102;18–28. doi:10.1136/heartjnl-2015-308044.

Neal ML, Kerckhoffs R. Current progress in patient-specific modeling. Brief Bioinform. 2010;11:111–26.

Perktold K, Gruber K, Kenner T, Florian H. Calculation of pulsatile flow and particle paths in an aneurysm-model. Basic Res Cardiol. 1984;79:253–61.

Raghavan ML, Vorp DA, Federle MP, Makaroun MS, Webster MW. Wall stress distribution on three-dimensionally reconstructed models of human abdominal aortic aneurysm. J Vasc Surg. 2000;31:760–9.

Richardson PD, Davies MJ, Born GVR. Influence of plaque configuration and stress-distribution on fissuring of coronary atherosclerotic plaques. Lancet. 1989;2:941–4.

Rybicki EF, Weis EB, Simonen FA. Mathematical analysis of stress in human femur. J Biomech. 1972;5:203–15.

Sherwin SJ, Karniadakis GE. A triangular spectral element method—applications to the incompressible Navier-Stokes equations. Comput Methods Appl Mech Eng. 1995;123:189–229.

Taylor CA, Figueroa CA. Patient-specific modeling of cardiovascular mechanics. Ann Rev Biomed Eng. 2009;11:109–34.

Thresher RW, Saito GE. The stress analysis of human teeth. J Biomech. 1973;6:443–4411.

Turner MJ, Clough RW, Martin HC, Topp LJ. Stiffness and deflection analysis of complex structures. J Aeronaut Sci. 1956;23:805–23.

Wang DHJ, Makaroun M, Webster MW, Vorp DA. Mechanical properties and microstructure of intraluminal thrombus from abdominal aortic aneurysm. J Biomech Eng. 2001;123:536–9.

Witherden FD, Farrington AM, Vincent PE. PyFR: an open source framework for solving advection–diffusion type problems on streaming architectures using the flux reconstruction approach. Comput Phys Comm. 2014;185:3028–40.

Xu C, Pham DL, Prince JL. 2000. Image segmentation using deformable models. In: Fitzpatrick JM, Sonka M, editors. Handbook of medical imaging, volume 2, Medical image processing and analysis. SPIE Press: Bellingham, USA; 2000. pp. 129–74.

Zienkiewicz OC. The birth of the finite element method and of computational mechanics. Int J Num Meth Eng. 2004;60:3–10.

Zienkiewicz OC, Taylor RL, Zhu JZ. The finite element method: its basis and fundamentals. 7th ed. Oxford: Butterworth-Heinemann; 2005.